Subsurface hydrothermal alteration mapping in the Reykjanes Geothermal area using a combined geoelectrical approach.

Lore Vanhooren *[α, β], Elien Vrancken[α], Warre Dekoninck[α], Adrian Flores-Orozco[γ], Olivier Fontaine[β], Bergur Bergsson[δ], Kristín Jónsdóttir[δ], Corentin Caudron[β], and Thomas Hermans[α]

[α] Laboratory of Applied Geology and Hydrogeology, Ghent University, Belgium.

[β] G-Time laboratory, Université libre de Bruxelles, Belgium.

[γ] Department of Geodesy and Geoinformation, TU-Wien, Austria.

[δ] Icelandic Meteorological Office (IMO), Reykjavik, Iceland.

Abstract

Most high-temperature geothermal areas have a similar resistivity signature, reflecting the alteration state of the system, as is the case for the Reykjanes high temperature system. A geothermal system has an intermediate resistivity core (30-100 Ωm), overlain by a low resistivity cap (1-10 Ωm), at Reykjanes this cap reaches the surface. Hence, the study of the shallow subsurface can provide insights into the state of the system and deeper processes. Traditionally, geothermal systems are studied using electromagnetic methods, which have a large penetration depth but a low resolution. This is sufficient to characterize the system, but capturing dynamics requires sufficiently large changes and careful survey design. In this study, we explore the potential of the combined use of three geo-electric methods: electrical resistivity tomography (ERT), induced polarization (IP), and self-potential (SP), to characterize the shallow (<50 m) subsurface at Reykjanes and interpret it in a dynamic context, without the need for repeated measurements. The observed resistivity signature reflects the typical resistivity distribution known at the site. The addition of SP allows the identification of active geothermal processes, which are highly variable and localized. The IP signal revealed a shallow (<20m) sealing structure, prohibiting fluid and gas migration, causing the absence of hydrothermal surface expressions. Such a seal can be potentially hazardous due to over-pressurization and could not be identified from resistivity imaging alone. Here we demonstrate that shallow structures can act as a proxy for deep processes, furthermore, we show that the combination of the tree methods is invaluable in studying these complex systems and recommend this for future studies.

Keywords: Alteration mapping; Shallow; Geo-electric; Reykjanes.

1 Introduction

Most volcanoes on Earth host a volcanic hydrothermal system (VHS), where complex interactions occur between the solid, liquid, and gas phases [Caudron et al. 2018a]. These VHS are of great importance as they can be exploited for geothermal energy [Volpi et al. 2003; Aizawa et al. 2009; Karlsdóttir et al. 2020] but also pose a significant safety hazard as they are related to gas- or phreatic eruptions [e.g. Caudron et al. 2018b; 2019]. The general structure of a VHS is well known, as it has been extensively studied for the exploration of geothermal potential. Resistivity methods are favoured for reservoir characterization because they are sensitive to the typical alteration sequence and hence reservoir structure [Arnason et al. 2000; Muñoz 2014]. However, the dynamics are less well understood, especially the changes leading up to phreatic eruptions. Pre-eruptive signals

* Lore.Vanhooren@UGent.be

have been identified, but they are not consistent between eruptions [Montanaro et al. 2022]. Geo-electric methods are sensitive to the presence of alteration clays [Lévy et al. 2018], temperature [Hermans et al. 2014], and saturation [Binley and Slater 2020], making them a feasible addition for VHS monitoring.

In this work, we explore the potential of geo-electric methods to delineate spatio-temporal variations of these parameters. Methods like self-potential (SP), electrical resistivity tomography (ERT), and induced polarization (IP) depend on the electrical properties of the subsurface, either as a passive signature (SP) or as a response to an applied electrical field (ERT/IP). They are sensitive to the presence of groundwater or groundwater flow, porosity, temperature, salinity, clay content, and mineral precipitations [Binley and Slater 2020], making them especially suited for studying hydrothermal areas and their related alteration. The advantage of geophysical methods is that they provide quasi-continuous temporal or spatial data, and they are non- to minimally invasive [Binley and Slater 2020]. The downside is that they are influenced by a large number of physical parameters which makes them difficult to use independently, especially in volcanic areas where many processes occur simultaneously. This can be overcome by combining different (geo-electric) methods [Ghorbani et al. 2018].

Although the Reykjanes peninsula has become volcanically active in recent years [Einarsson et al. 2023; Troll et al. 2024], our study area, the Reykjanes geothermal system, has not been subject to eruptive activity. However, it hosts an active hydrothermal system expressed at the surface as boiling mud pools, steam vents, and fumaroles. Characterization of the geothermal system has been done using magneto telluric (MT) and transient electromagnetic (TEM) [Karlsdóttir et al. 2020]. However, monitoring attempts remain inconclusive [Darnet et al. 2019], a detailed overview of the resistivity structure is given in section 2. Characterization and monitoring using other resistivity methods such as ERT or IP has not been explored there. Because the top of the geothermal system cuts the surface at Reykjanes, shallow observations can provide direct insights into the state of the geothermal system with the advantage of having a high resolution.

In this contribution, we present a characterization of the shallow geothermal field where pressurization can occur through sealing [e.g. Christenson et al. 2010; Ardid et al. 2021], using SP, ERT and IP. The combination of the three methods has proven to be valuable in the study of hydrothermal systems [Troiano et al. 2021; Revil et al. 2023b], which is essential for hazard assessment. Similarly to the work done by Troiano et al. [2021], characterization of the shallow subsurface in Reykjanes enables us to identify areas of activity that are not visible from the surface. These observations highlight the potential of monitoring deep activity from shallow measurements. Although we use preliminary monitoring of the site to identify potentially active areas, long-term monitoring will be presented in future contributions.

2 Geology and Geothermal setting

Due to its geodynamic context, Iceland is mostly made up of basalts. The neovolcanic zone (Figure 1) marks the youngest rocks and active volcanism on Iceland, dividing older rocks east and west from the active spreading centre [Sigmundsson et al. 2020]. The spreading rate at the mid Atlantic ridge (MAR) has been estimated between 18 and 20 mm/y using ocean floor reversal patterns [Demets et al. 1994] and GPS measurements [LaFemina et al. 2005]. The island is characterized by a complex plate deformation zone caused by the interaction between the plate boundary and hotspot, the MAR splits into a series of sub-areal and submarine rift- and transform segments [Einarsson 2008]. Sæmundsson et al. [2020] defines the four

main tectonic structures as spreading zones, fracture zones, trans-tensional (oblique) zones, and flank zones. Most volcanism occurs in spreading zones but is also present in the oblique zones, as is the case on the Reykjanes peninsula. Iceland presently hosts three active rift segments: the Reykjanes-Langjökull Rift Zone, the Eastern- and Northern Rift Zones [Khodayar et al. 2018].

The Reykjanes Ridge (RR) segment of the MAR continues onshore on the Reykjanes Peninsula (RP). Both on- and offshore segments are arranged in a sub-parallel, staggered manner, but are distinguished by a different strike direction [Clifton and Kattenhorn 2006; Pałgan et al. 2017]. These sub-parallel fractures are characteristic of volcanically active areas [Thordarson and Höskuldsson 2008] and form the main structural feature within the RP [Khodayar et al. 2018]. The RP rift splits into narrower, parallel fissure swarms, each hosting a volcanic system. Historically, five systems are defined (from west to east): Reykjanes, Eldvörp-Svartsengi, Krýsuvík, Brennsteinsfjöll, and Hengill [Clifton and Kattenhorn 2006]. Recently, a sixth volcanic system, Fagradalsfjall, has been defined, situated between Eldvörp-Svartsengi and Krýsuvík [Sæmundsson et al. 2020]. The RP has become volcanically active again after 800 years of rest [Sæmundsson et al. 2020] marked by periodic eruptions of Fagradalsfjall in 2021, 2022 and 2023 [Einarsson et al. 2023; Krmíček et al. 2023] and Svartsengi in 2023, 2024 and 2025 [IMO 2024; Troll et al. 2024]. Our study area is located on the Reykjanes high temperature field (Figure 1), 25 km west of Fagradalsfjall and 15 km west of Svartsengi, and has not exhibited volcanic activity since the onset of the new episode.

Fissure swarms within the neo-volcanic zone are often host to central volcanoes and their associated high-temperature geothermal systems. The heat source can either be a magmatic intrusion or a cooling magmatic body from an old eruptive episode [Eysteinsson et al. 1994]. Most high-temperature geothermal systems have a similar resistivity signature [Eysteinsson et al. 1994; Flóvenz et al. 2012]. Close to the surface, basalts are cold and unaltered with high resistivity (1000 Ωm), which is several orders of magnitude higher in dry conditions. A low resistivity cap (1-10 Ωm) can be found underneath, coinciding with the smectite-zeolite alteration zone. Smectite has a high cation-exchange capacity (CEC), causing the low resistivity in this zone [Lévy et al. 2018]. Here the surface conductivity is the main conductive mechanism dominating over the electrolytic conductivity. The cap covers an intermediate resistivity core (30-100 Ωm), coinciding with a change in alteration minerals to chloride-epidote. Mixed-layer clays have a lower CEC [Deer 1978], here, the conductivity is primarily controlled by a combination of surface and electrolytic conductivity. Alteration sequences correspond to specific temperature intervals, the smectite-zeolite zone occurs in the temperature range of 110-220°C, the chlorite-epidote zone at temperatures between 220-240°C. Consequentially, resistivity can be used as a geo-thermometer in basaltic high temperature systems. Historically, DC resistivity methods like ERT were deployed to map the geothermal structure [Arnason et al. 2000]. Currently, the joint use of transient electromagnetics (TEM) and magneto-tellurics (MT) is preferred due to its higher depth penetration [Árnason 2015] and has been successfully deployed to characterize high temperature geothermal systems in Iceland, including Krafla, Hengill [Gasperikova et al. 2011; Rosenkjaer et al. 2015], Krýsuvík [Hersir et al. 2020], Reykjanes, Eldvörp, and Svartsengi [Karlsdóttir et al. 2020].

The Reykjanes geothermal area differs from the classic resistivity signature due to the high salinity of the geothermal fluid, with fluid chemistry dominating over the alteration signal. Hence, the contribution of the electrolytic conduction becomes increasingly important with higher salinities. Eysteinsson et al. [1994] reported no observable resistivity layering in brine

systems, however, more recent studies identified the expected resistivity layering albeit with lower values, in the range of 1-3 Ωm for the low resistivity cap and 10-30 Ωm for the intermediate resistivity core [Friðleifsson et al. 2003; Karlsdóttir et al. 2020] (compared to 1-10 Ωm and 30-100 Ωm respectively) . The low resistivity cap reaches the surface along an area of approximately 1 km^2, with intense hydrothermal surface manifestations such as steam vents, mudpools, and fumaroles [Björnsson et al. 1970]. Furthermore, there is history of episodic hydrothermal explosions in this area [Friðleifsson et al. 2003]. A large-scale 3D resistivity model was published by Karlsdóttir et al. [2020] based on the joint inversion of MT and TEM data, they found that the cap is made up of connected low resistivity anomalies rather than a continuous zone. Additionally, the model reveals an area of lower resistivity within the high-resistivity core, which is suggested to be a zone of higher permeability and temperature, facilitating the circulation of hydrothermal fluids. A low resistivity zone is commonly present at depth, commonly found around 3-5 km, originating from the heat source, however, this feature can not be resolved from the resistivity distribution, potentially due to different tectonic settings [Sigurdsson 2010; Karlsdóttir et al. 2020]. Characterization surveys were mainly conducted for the utilization of the natural resources of the geothermal field by field operator HS Orka [Friðleifsson et al. 2020]. The field has also been studied extensively as a potential site for the Icelandic Deep Drilling Project (IDDP) [Friðleifsson et al. 2003]. Resistivity methods have also been deployed to assess the effect of the exploitation of the geothermal field. Controlled-Source EM (CSEM) measurements were repeated prior to and after the installation of the IDDP2 well [Darnet et al. 2019; Bretaudeau et al. 2021], joint inversion with MT data revealed no significant difference. Darnet et al. [2019] suggest that only changes over a significant reservoir volume can result in detectable signal, furthermore, inadequate repeatability between the measurements introduces error in the timelapse analysis. Successful monitoring attempts using CSEM have been made in VHS, where changes in the order of 10-20 % have been observed given carefull survey design to minimize the repeatability error [Minami et al. 2018]. Magnusdottir and Jonsson [2020] proposed a new method to monitor the state of the geothermal field by utilizing the borehole casings as long electrodes in a DC resistivity survey. Measuring the resistance difference between different combinations of boreholes enables fracture connectivity and field productivity to be determined.

The Reykjanes geothermal field is unique in Iceland because the fluid recharge of the hydrothermal system is 100% seawater. Other systems in the proximity of the ocean always have at least a small fraction of freshwater recharge, like the Svartsengi system [Kadko et al. 2007; Friðleifsson et al. 2020]. Silica, calcium and potassium levels are increased, which can be caused by the dissolution of the basaltic host rock. Sulphur and magnesium are depleted, likely due to the deposition of secondary minerals [Arnórsson 1995]. Because of its fully seawater-recharged nature, the Reykjanes system is considered an on-land black smoker analog, though under low hydrostatic pressure, and has been studied extensively in this context [Marks et al. 2010; Fowler et al. 2015; Friðleifsson et al. 2020]. The host rocks are young, highly permeable basalts [Björnsson et al. 1970], hydrothermally altered due to the presence of the high-temperature field. Geological logs show a progressive hydrothermal alteration with increasing depth, described in detail by Marks et al. [2010]. Mineral assemblages suggest the alteration sequence has a composition transitional between a Mid Ocean Ridge basalt and an Ocean Island Basalt [Marks et al. 2010]. Due to its high permeability and the heavily fractured nature of the basalt, rainwater infiltrates in the shallow subsurface

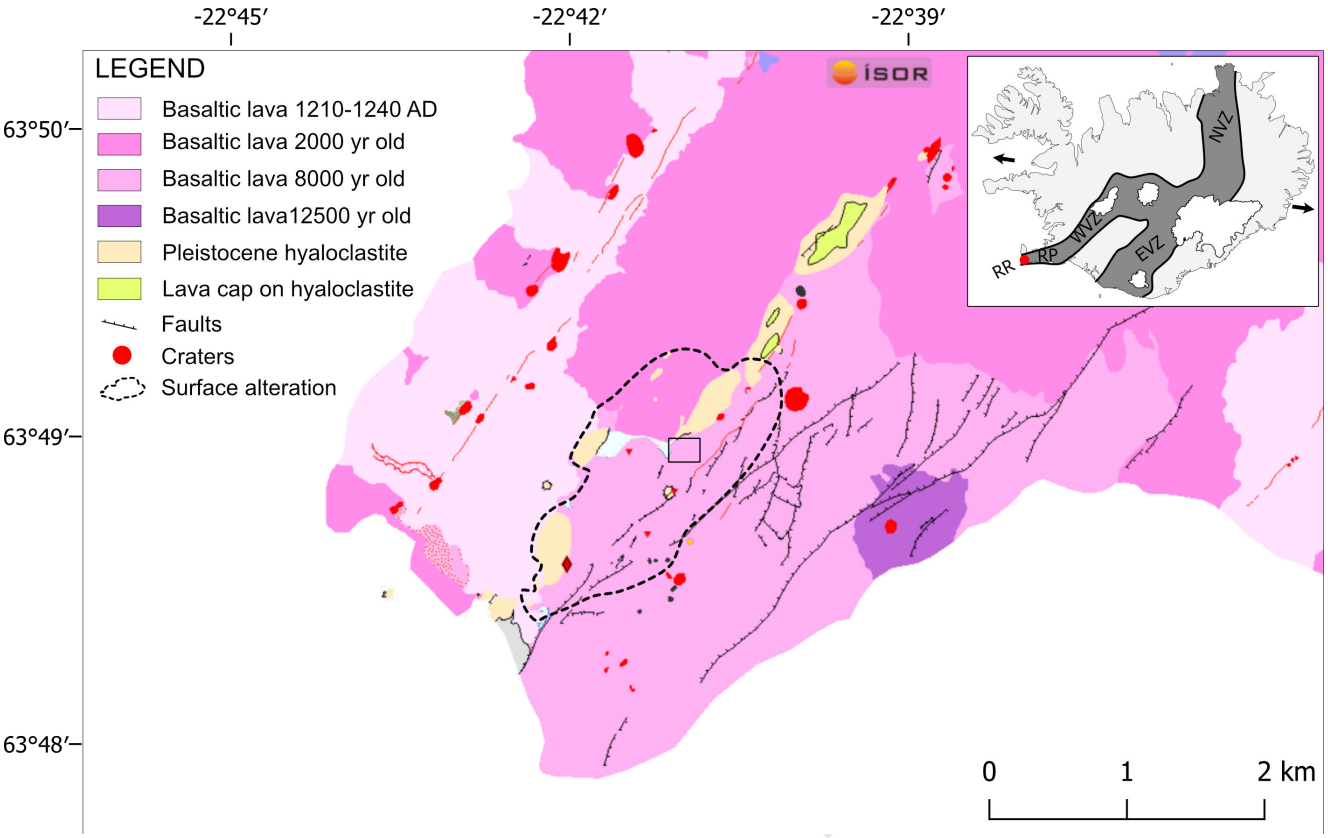

Figure 1: Geology of the Reykjanes Peninsula, adapted from Sigurdsson [2010]. The study area is marked by the black square in the center of the alteration zone. The neovolcanic zone is indicated on the map of Iceland with its main tectonic elements: Reykjanes Ridge (RR), Reykjanes Peninsula (RP), and the Western, Eastern, and Northern Volcanic zones (WVZ, EVZ, NVZ).

forming a thin freshwater lens on top of the chemically altered seawater. In the Reykjanes area, the freshwater lens has a thickness of approximately 30 meters, increasing landward, reaching 60 meters at Svartsengi [Sigurðsson 1986].

3 Geophysical Methods

3.1 Electrical Resistivity Tomography and Induced Polarization

Electrical resistivity (ρ) is a measure of the ability of a medium to allow the flow of electrical current, which is inversely related to the electrical conductivity (σ). It can provide valuable information about the hydrological and geological properties of the subsurface [Loke et al. 2013]. Resistivity is sensitive to, amongst others, porosity, salinity, saturation, temperature, and the presence of (semi) conducting minerals and clays. It has been applied on volcanoes to characterize their structure and associated hydrothermal system and to image the presence of hot conductive fluids [Rosas-Carbajal et al. 2016; Troiano et al. 2019]. While resistivity provides information about how well a medium can conduct current, chargeablility represents the ability to store electrical charges. Charges are retained as a result of polarization at the interface between grain and electrolyte in the so-called electrical double layer (EDL). In case of metallic minerals, the polarization of charges also takes place within the matrix [Binley and Slater 2020], hence the method is commonly known as Induced Polarization (IP). IP is sensitive to the presence of sulfides, iron-oxides [Pelton et al. 1978; Gurin et al. 2015] and clay minerals like smectite [Weller et al. 2013] which

are common alteration minerals in magmatic-hydrothermal systems [Meunier 2005], making the method especially well suited for alteration mapping [Revil et al. 2002; Ghorbani et al. 2018].

An ERT measurement involves the injection of an electrical current between two electrodes (A and B) and the subsequent measurement between two different electrodes (M and N). A section is computed through the inversion of data collected with different combinations of electrodes (quadrupoles). Quadrupoles can be arranged in different formations, influencing the depth of investigation, horizontal and vertical resolutions [Dahlin and Zhou 2004]. IP can be measured in the time domain (TDIP) or frequency domain (FDIP), in this study, the former is used by measuring the voltage decay after an applied current. On the field, ERT and IP measurements are done subsequently, resistivity is measured before voltage shutoff. IP windows are measured at set intervals following a delay after the voltage shutoff. Such a delay is commonly used to reduce the contamination of the data due to parasitic electromagnetic fields, like electromagnetic or inductive coupling [Dahlin et al. 2002; Flores-Orozco et al. 2018].

3.2 Self Potential

The self-potential (SP) method is a passive technique that studies the electrical fields in the Earth by measuring the electrical potential. It is well established in the study of volcanic hydrothermal systems due to its sensitivity to fluid flow, oxidation-reduction processes, temperature, and concentration gradients [Revil et al. 2023a]. SP signals are generally positive in the flow direction, hence uprising fluids generate a positive anomaly [Revil et al. 2002], as a result, a typical w-shaped anomaly is often present over the summit of a volcano, constraining the hydrothermal system [Revil et al. 2008; Aizawa et al. 2009; Revil and Jardani 2013]. Other volcanological applications include constraining structural features like fracture systems [Di Maio et al. 1998] and edifice stability [Chaput et al. 2019]. As the SP method is passive, it can be limited by weak signals or the discrimination of different processes underlying the recorded data.

To avoid polarization effects at the electrode surface, SP is measured at the ground surface, between two non-polarizable electrodes consisting of a metal rod submersed in a saturated solution of the corresponding salt, housed in a porous container to facilitate electrical contact [Lowrie 2007]. An SP profile consists of a base station, which is the reference point and is artificially set a 0 mV. Measurements are performed between the fixed electrode at the base station and a moving electrode. In this study, the moving electrode is measured three consecutive times at each station to assess the measurement error. When the connecting cable reaches its full range, a new base station is set to continue profiling [Barde-Cabusson et al. 2021; Revil et al. 2023a]. For generating large maps, profiles are measured in closed loops, meaning a return to the base station at the end of the profile to check for the existence of a closure error. Since all measurements are relative to an artificially set base, the potential itself becomes meaningless hence, interpretation should be strictly qualitative [Revil et al. 2008].

4 Data and Processing

4.1 Field Survey

On the field, ERT and IP profiles were measured in a cross-hatched pattern (Figure 2). The profiles are 355 m long, consisting of 72 electrodes with a 5 m spacing, and are measured using the multiple gradient (MG) protocol, known for its good compromise

between resolution and good signal-to-noise ratio [Dahlin and Zhou 2006]. Stacking was limited to two stacks to reduce the polarization at the electrodes. Measurements are done using the *Syscal Pro* from IRIS instruments, injecting for 1s using a 50% duty cycle. IP windows are measured in 20 semi-logarithmically ordered time windows, after a 40 ms delay. Stainless steel electrodes are mounted in the surface, and where necessary, clay was used to ensure good electrical contact. Processing and inversion of the ERT and IP data are discussed in Section 4.2.

Since ERT is sensitive to temperature, eight TOMST temperature and soil moisture sensors [Wild et al. 2019] were installed along profile 1, two *extreme* sensors, which can accurately measure temperatures up to 80°C, and six *long* sensors, which can be buried up to 40 cm in the soil. The temperature is measured at three locations, in the air, at the soil-air interface, and in the soil [Wild et al. 2019].

The SP survey was conducted at the same electrode locations as the ERT lines but not simultaneously, to avoid polarization effects. Measurements were done using the total-field method because it has a lower cumulative error compared to the gradient method and provides more flexibility during measurements, making it better suited for difficult terrains [Lowrie 2007]. To ensure good electrical contact, the electrodes were mounted in shallow holes (5-10 cm) filled with a bentonite-salt slurry [Robert et al. 2011]. On the field, the connecting wire had a length of only 30 m, requiring frequent relocation of the base station for SP measurements. Processing involves a correction at each base station to ensure continuity of the signal and a correction for the drift, which is estimated as a linear interpolation from the multiple base measurements [Revil et al. 2023a]. Since the profiles are arranged in a cross-hatched pattern, three points of intersection were used to perform an additional in-between profile drift correction, using the profile with the most stable signal as a baseline. The closing error at the last intersection point is used to assess the level of error on the relative SP signal.

4.2 Signal Processing and Inversion

4.2.1 *Error considerations and Reciprocal measurements*

Misinterpretation of ERT images can be prevented with accurate quantification of the measurement error or noise [Labrecque et al. 1996]. The defined noise level can have a big influence on the tomograms as an overestimation can result in over-smoothing of the resistivity whilst an underestimation can introduce artifacts in the inversion [Hermans et al. 2012]. A common way to estimate the noise level in ERT is by measuring the reciprocal profile. Relying on the principle of reciprocity, when the current and potential dipoles are interchanged, the resulting response should be identical, given a linear [Parasnis 1988], but not necessarily homogeneous [Labrecque et al. 1996] behavior of the subsurface.

The reciprocal error is defined as $e_{N/R} = R_N - R_R$ with R_N and R_R representing the normal and reciprocal resistance, respectively. Slater et al. [2000] propose an error model where the reciprocal error increases linearly with the average resistance:

$$|e_{N/R}| = a + bR \tag{1}$$

where a represents the absolute error, in Ω, and b is a relative increase with the resistance. The parameters can be determined by the envelope function as proposed by Slater et al. [2000]. This approach overestimates the error in all data points, which will result in an over-smoothed conservative image. Alternative approaches derive a less conservative error

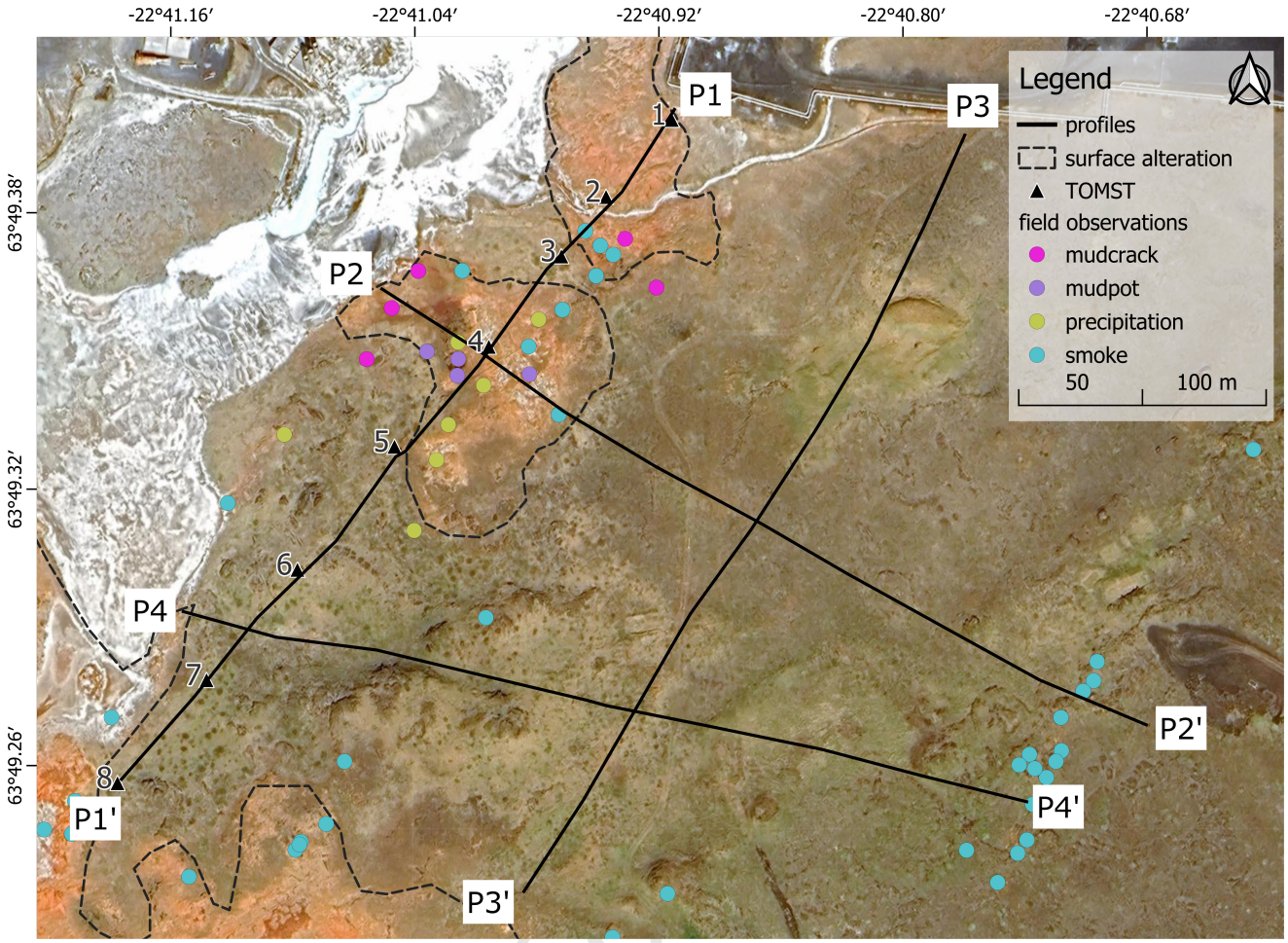

Figure 2: Localization of the geophysical profiles (ERT/TDIP/SP) and surface observations in the Reykjanes Geothermal Field. The profiles are measured from North to South and West to East. The surface alteration is delineated using Google imagery combined with field observations.

model by balancing over- and underestimation of the error, allowing the recovery of more detail in the resulting image [e.g. Koestel et al. 2008]. Here we use a linear regression model based on a least-square fit [Van Riet et al. 2022].

4.2.2 *Data Processing*

The ERT data processing is limited to removing negative values and bad datapoints based on the reciprocal data described above. The reciprocal approach can also be used for the TDIP data but is not sufficient to identify outliers and readings with poor S/N ratios. TDIP measures the voltage drop as a decay curve, the apparent chargeability is calculated as the area under the decay curve [Binley and Slater 2020]. Hence all curves that show erratic or non-decaying behaviour are rejected. Additionally, curves that asymptotically decay towards a non-zero value are rejected as well [Evrard et al. 2018; Thibaut et al. 2021]. This decay curve analysis is common practice in processing TDIP signals [Evrard et al. 2018] and relies on the fitting of a decreasing exponential or power function to the data [Flores-Orozco et al. 2018]. An rms-error is calculated between the measured and fitted data, all curves that do not meet a predefined threshold value are rejected. Here we use an exponential function with a threshold of 60%.

4.2.3 *Inversion*

The inverse electrical problem is ill-posed, meaning that there is no unique model to explain the data. Adding constraints to the inversion algorithm can contribute to finding a physically plausible model [Tikhonov and Viak 1977]. This is done by minimizing the objective function of a regularized problem:

$$\psi(m) = \psi_d(m) + \lambda\psi_m(m) \tag{2}$$

with $\psi_d(m)$ the data misfit, $\psi_m(m)$ the model misfit and m the inverted parameter. The regularization parameter λ quantifies the compromise between the two terms. The data and model misfit can be expressed in terms of their operators, the objective function can be rewritten as [Kemna 2000]:

$$\psi(m) = ||W_d(d - f(m))||^2 + \lambda(||W_m(m - m_0)||^2 + \alpha||m - m_0||^2) \tag{3}$$

The first term of Equation *4.2.3* regards the data misfit, with W_d the data weighing matrix, a diagonal matrix with $1/\epsilon_i$ as elements. The standard deviation ϵ is commonly quantified by the noise level using the reciprocal measurements (Section *4.2.1*). The regularization term consists of two elements, a smoothness constraint where W_m is a matrix evaluating the roughness of m, and a smallness constraint ensuring that the model does not deviate too much from a reference model m_0. The smallness constraint utilizes a closeness factor α, weighing the importance of the reference model [Dumont et al. 2016].

The objective function is minimized iteratively through a Gauss-Newton scheme using CRTomo [Kemna 2000]. The regularization parameter λ is optimized at each step through a line search, minimizing the error weighted root-mean-square-error (ϵ_{RMSE}) until the ϵ_{RMSE} reaches a value of 1, meaning that the data is fitted to its estimated noise level.

The addition of the smallness constraint allows the user to include some a priori information which is known to improve the inversion result [Oldenburg and Li 1994; Caterina et al. 2014; Hermans 2014]. In practice, a background resistivity value can be defined for each cell of the reference model, note that the choice of background resistivity and the closeness factor can introduce some subjectivity in the inversion [Hermans et al. 2014]. A homogeneous background resistivity is used, of 1 Ω with a weighing factor of 0.01 for each cell. The low resistivity was chosen to reflect the nature of the field site, where the combination of high temperature and high salinity will result in a very conductive subsurface at depths larger than 10 m.

CRTomo solves for the distribution of the natural logarithm of the complex resistivity $m = \rho^*$, calculations are expressed in terms of the amplitude of the resistivity and the phase shift ϕ. The measured TDIP data consists of chargeability measurements that need to be converted to the phase shift in the frequency domain in order to execute inversion [Kemna 2000; Thibaut et al. 2021]. After inversion, the phase shift is back-transformed to chargeability. Because the chargeability is closely related to the resistivity, the latter can have a significant impact on the measured chargeability. Hence to isolate the polarization effect, the chargeability can be normalized by the resistivity $MN = M/\rho$ [e.g Lesmes and Frye 2001; Benoit et al. 2019]. TDIP datasets are often heavily filtered and can result in a significant loss of data, this is much less so with resistivity. Therefore,

Table 1: Inversion statistics. The number of iterations and RMSE are given for the independent resistivity inversion and inversion including the phase shift.

Profile	Resistivity		Phase	
	# it.	ϵ_{RMSE}	# it.	ϵ_{RMSE}
1	5	0.9971	7	0.0358
2	6	0.9953	9	0.0303
3	7	0.9960	7	0.0329
4	7	0.9948	7	0.0513

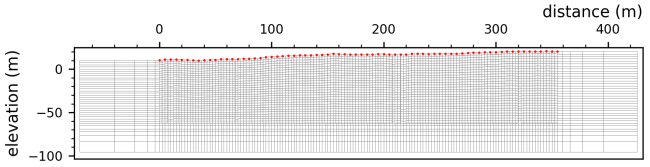

Figure 3: Inversion mesh of profile 4, containing 152 columns and 35 rows, resulting in 5320 cells. Electrodes are indicated by the red dots; one node is added between each electrode pair to optimize the resolution.

the resistivity datasets are first inverted independently, i.e., without including the phase shift, followed by an inversion of the complex resistivity for the IP dataset. Table 1 reports the number of iterations needed for both inversions and the ϵ_{RMSE} reached upon convergence. The resistivity column refers to the independent resistivity inversion. For the inversion including the phase, only the ϵ_{RMSE} of the phase parameter is reported.

When inverting field data, a topographic effect can be present in the inversion, which may distort the recovered resistivity distribution [Tsourlos et al. 1999; Mansourian et al. 2023]. This is accounted for in the inversion algorithm; the mesh nodes are shifted upwards to approximate the field topography, and subsequently, the real geometric factors are computed prior to inversion. The grid is extended laterally and at depth to account for boundary effects, the mesh construction is illustrated in Figure 3 and is the same for all four profiles with their corresponding topography. Assessing the quality of the inverted image is of vital importance for the interpretation of the data [Caterina et al. 2013]. Here we apply the cumulative sensitivity matrix [Kemna 2000], which is representative of how well the data is resolved in the inversion model [Paepen et al. 2022].

5 Results and Discussion

5.1 Data Quality and Error Quantification

The measured resistances are distributed between 0.0001 and 3 Ω (Figure 4), the distribution of profile 1 is skewed to the left with a significant peak between 0.0001 and 0.001 Ω, profiles 2 and 4 are skewed to the right. The average resistance of profile 1, 0.13 Ω, is significantly lower than the other profiles, approximating 0.80 Ω. This is reflected in the reciprocal data filtering, the method removes points where the two measurements deviate 10% from each other (Table 2). This will have a larger effect on smaller values because of the presence of some systematic noise, (Figure 5). On profile 1, 73.96% of the data is retained after filtering, on the other profiles significantly more data is retained (Table 2). A global error model was determined by reconstructing a trendline on the remaining points. The analysis was done on all profiles simultaneously to deduce a

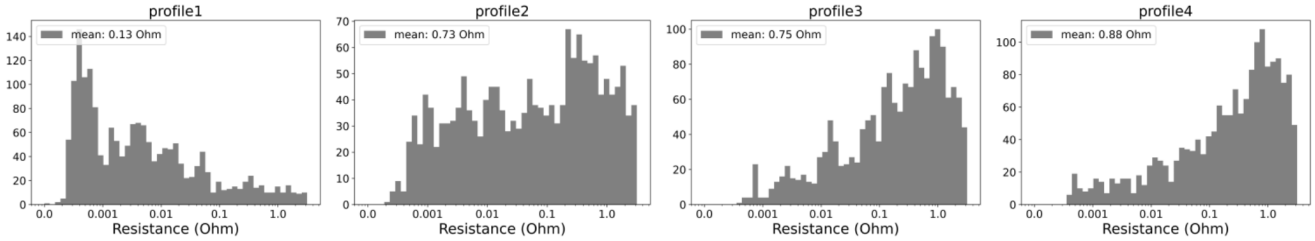

Figure 4: Resistance distribution in the four profiles, the resistance is plotted logarithmically.

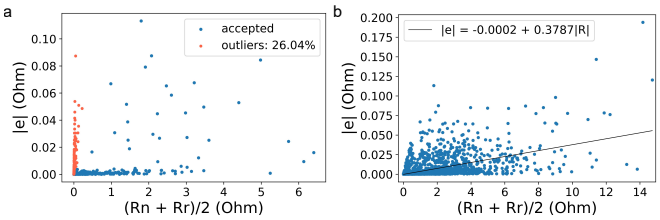

Figure 5: a: example of the data filtering for profile 1, outliers are determined based on the normal/reciprocal discrepancy, with the average resistance plotted against the residual error $|e|$. The orange dots represent the points filtered out using the method described by Slater et al. [2000]. b: global error model reconstruction (black line) fitted on the accepted points of the four profiles combined.

single linear error model with parameters $a = -0.0002$ Ω and $b = 0.38\%$. The a factor originates from the regression and is unrealistic, given the underlying numerical error of CRTomo [Flores-Orozco et al. 2012], a value of 0.001 Ω was used instead.

IP data is processed by decay curve analysis involving curve-fitting to filter out most of the erratic curves as shown for profile 1 (Figure 6). Using a stricter threshold, for example, 0.75 instead of the used 0.60 would improve the outcome. However, profile 1 already has a low acceptance rate, where only 29.85% of the data were retained after the analysis, increasing the threshold would result in an even sparser dataset for inversion. Profiles 2, 3, and 4 have a substantially higher acceptance rate (Table 2). The areas where more data is rejected overlap with the low resistance (Figure 7), which can be attributed to the presence of high-salinity groundwater at depth [Binley and Slater 2020] which reduces the signal-to-noise ratio [Cong-Thi et al. 2024].

5.2 Inversion Results

The inversion results are reliable in the top layer of the model as can be seen in Figure 8, the sensitivity shows the data is well resolved in the upper 20 to 30 meters. The inversion results are shown with the self-potential data (Figure 9). All four profiles show a zone of high resistivity (50-600 Ωm) at the surface of maximum 20 and minimum 10 m thickness. The high resistivity zone is bound at the bottom by low resistivity (1-10 Ωm). The low resistivity reaches the surface in some profiles,

Table 2: Percentage of accepted data after the filtering steps for the resistance and chargeability data, i.e. the proportion of data used for inversion.

Profile	Resistance (%)	Chargeability (%)
1	73.96	28.69
2	89.78	72.10
3	96.85	84.91
4	97.23	87.15

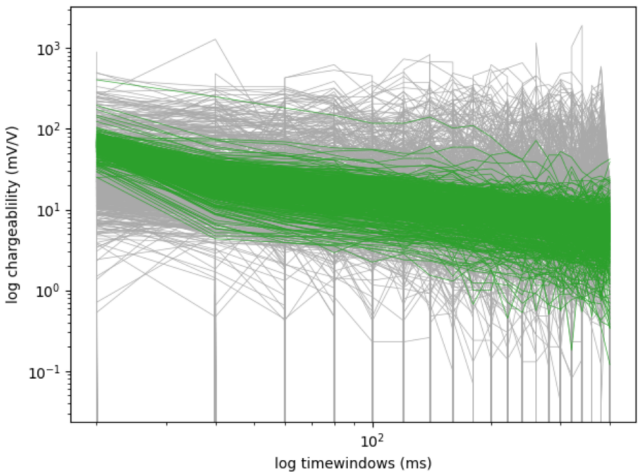

Figure 6: Example of the decay curve analysis for profile 1, a curve is accepted (green lines) when it deviates no more than 60% from a fitted exponential function. Note that the vertical lines represent negative values as they cannot be shown logarithmically.

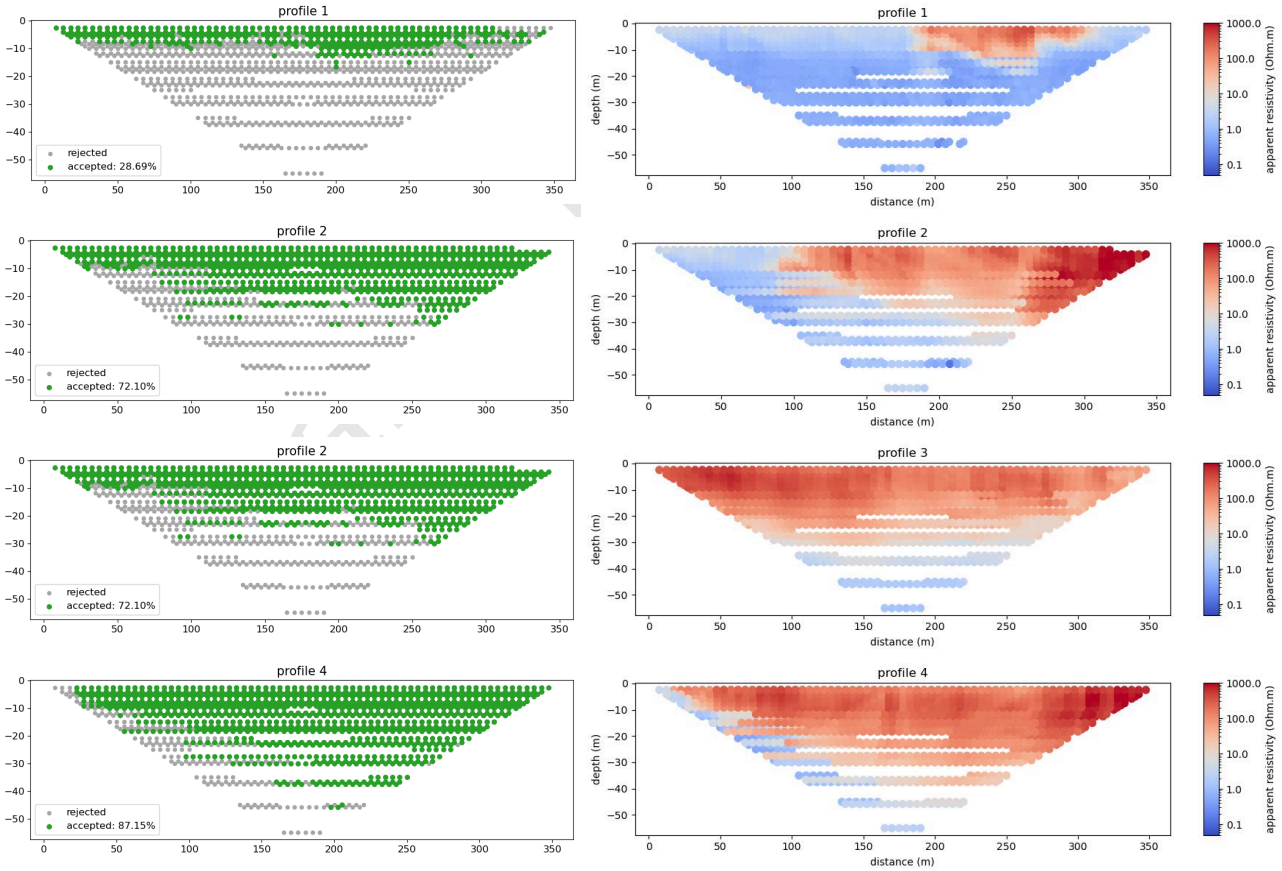

Figure 7: Acceptance rate of the decay curve analysis plotted as a pseudosection, plotted alongside the apparent resistivity, areas where points are rejected coincide with low Resistance.

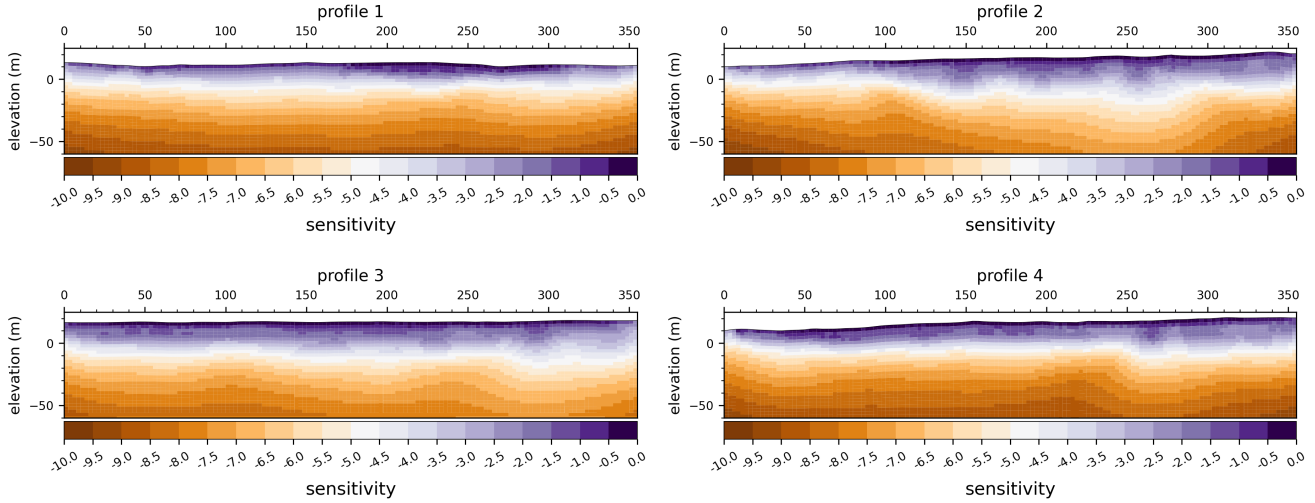

Figure 8: The sensitivity of the four profiles based on the resistivity inversion, a high value reflects that the data is well resolved in the inversion model.

on profile 1 between 0-180m and 310-400m, on profile 2 between 0-90 m and on profile 4 between 0-5m. The depth where the groundwater becomes saline according to Sigurðsson [1986] coincides with the model sensitivity. The high conductivity leads to a strong signal decrease at depth, which impacts the reliability of the inversion. The areas where the low resistivity reaches the surface coincide largely with the observation of surface alteration but not completely.

Due to the highly conductive nature of the subsurface, the majority of the deep data points (<30m) were removed from the IP dataset as the IP signal is below the noise level. The remaining dataset is sparse and is dominated by the points with a higher resistivity for which the voltages, and thus the signal-to-noise ratio, are larger. After inversion, the chargeability is increased in the top 20 m for the four profiles (10-30 mV/V). The normalized chargeability is also shown in order to isolate the polarizable areas. For profile 1, the normalized chargeability increases between 0 and 150m, and between 290 and 330m, with values ranging from 3 to 10 mS/m. On profile 2, increased normalized chargeability is present between 0-100 m, ranging between 2-4 mS/m, slightly lower than the anomaly in profile 1. Profiles 3 and 4 have no observable anomalies in normalized chargeability.

Given the nature of the SP method, the absolute value of the measurements should be disregarded and only trends and relative variations should be interpreted. The first part of profile 1 (0-150m) is erratic, with many fluctuations of the signal, there is a general trend of a plateau until 60m followed by a decrease until 150m. After that, the signal increases and follows a smooth concave trend between 180 and 280m, coinciding with the high resistivity area. The last part is characterized by an increase towards a plateau. Profile 2 has an increasing signal between 0-100m, reaching a relatively stable plateau until 260m. The last part has two big peaks, from 260-280m and from 300-340m. Profile 3 is relatively smooth with the absence of strong fluctuations, between 80 and 250 m there is a subtle concave feature. A stronger concave feature is present between 280 and 320 m. Profile 4 starts with a generally decreasing signal between 0 and 60 m, followed by a strong peak between 60 and 90m. The remainder of the profile is relatively stable with a few smaller peaks.

Table 3 shows the temperature gradients in the soil calculated from the TOMST sensors. The gradient is calculated between the soil and surface sensor, and given as an increase in °C per cm. The *XTreme* sensors are installed on the areas

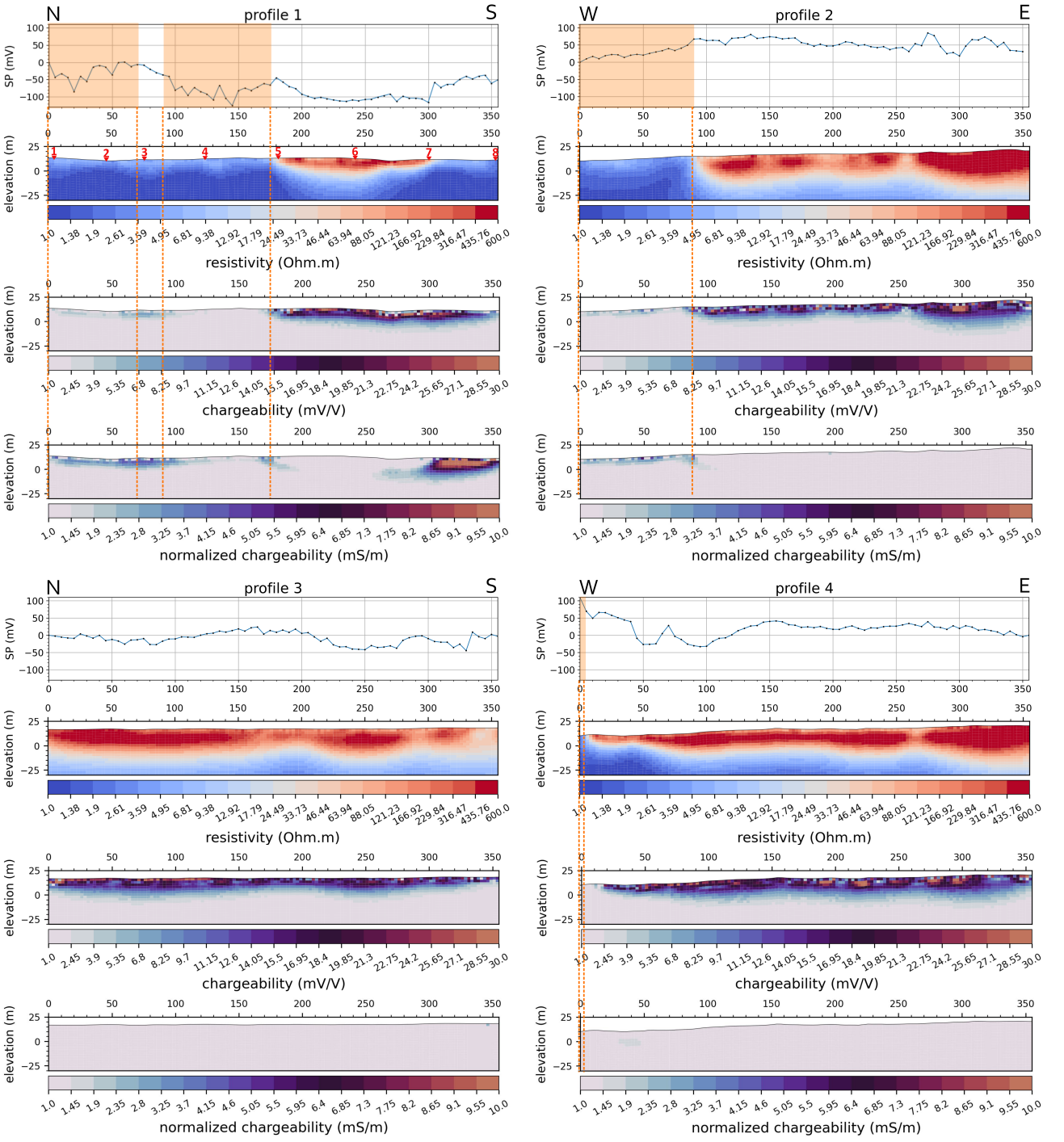

Figure 9: The results from the field campaign, for each profile, there is the corrected SP signal in mV, the resistivity in Ωm, the chargeability in mV/V and the normalized chargeability in mS/S. The orange-shaded areas and extended dashed red lines indicate where surface alteration was observed (Figure 2).

Table 3: Temperature measurements on 30/10/2022 at 8:00, the sensor locations are indicated on Figure 2. The temperature gradient is calculated between the soil and surface sensors, note that the surface sensor of the *XTreme* type is just under the soil surface, for the *long* type at 12.5 cm depth, hence the term surface temperature does not apply but should be seen as shallow soil temperature.

Sensor id	Sensor Type	Soil Temperature (°C)	Gradient (°C/cm)	Atm. Temperature (°C)
1	*Long*	46.50	1.53	6.63
2	*XTreme*	55.75	5.58	8.13
3	*Long*	25.25	0.64	7.06
4	*XTreme*	64.00	6.56	8.25
5	*Long*	34.13	0.72	6.90
6	*Long*	23.62	0.42	5.90
7	*Long*	19.25	0.27	5.87
8	*Long*	17.25	0.47	6.00

with the most intense surface activity, and have a very steep temperature gradient of more than 5°C/cm. The remaining sensors have a lower gradient, between 0.27 and 0.72 °C/cm with the exception of sensor 1 with an intermediate gradient of 1.53°C/cm. Table 3 also shows that where the soil temperature is high, the atmospheric temperature is elevated as well, indeed the atmospheric temperature is around 6°C for most of the sensors but around 8°C where the soil temperature is high. Hence heat radiates from the surface and can still influence temperature at 15cm above surface level.

5.3 Discussion

5.3.1 *Resistivity Zoning*

The resistivity distribution is typical of that of a seawater brine high-temperature geothermal system [Eysteinsson et al. 1994]. A high resistivity zone (50-600 Ωm) is overlying a low resistivity cap (1-10 Ωm). Karlsdóttir et al. [2020] reported that the low resistivity cap consists of smaller, intercalated lenses rather than a continuous layer, reflected by the shallow (< 30m) low resistivity. Here, the cap reaches the surface, reflected by intense surface alteration present on profiles 1 and 2. The high resistivity zone is described in literature as cold, unaltered basalt [Eysteinsson et al. 1994], heterogeneity present in the ERT images points to zones within this stable block that have been subject to more progressive alteration. Resistivity alone solely provides information on the historically most progressive state of alteration [Karlsdóttir et al. 2020]. The addition of SP allows for the identification of whether these conduits are hydrothermally active or have been abandoned, as a positive SP anomaly corresponds to upflow of hydrothermal fluids [Grobbe and Barde-Cabusson 2019]. On profiles 2 and 4, at 260m, a positive SP anomaly corresponds to a lower resistivity (120 Ωm), meaning the hydrothermal fluids percolate towards the surface. Similar resistivity features in the absence of the SP anomaly indicate zones of past activity. Notably, the identified active fluid pathways do not always correspond to surface manifestations like steam vents. The low resistivity cap is also prone to heterogeneity in the SP signal, with strongly varying signals. Water and gas likely follow complex flow paths linked to open and sealed fractures, which can potentially explain the strongly varying SP signal but cannot be confirmed with the available data. The low resistivity at depth (> 30 m) is a consequence of the thermal brine and corresponds to the depth where the saltwater interface has been identified. Sigurðsson [1986] reports a sharp interface, but a gradual transition is observed in the ERT which can be explained by smoothing effects of the regularization.

The variation in temperature gradients and the presence of the high gradient in sensors 2 and 4 are not uncommon in volcanic hydrothermal systems [e.g. Chiodini et al. 2005]. Chiodini et al. [2005] measured shallow (up to 40cm) vertical soil temperature profiles in the Solfatara crater and classified the resulting curves into four categories based on the gradient and shape of the curve. These differences are mainly caused by the initial gas concentration and the flux. In the Reykjanes field, degassing is primarily controlled by local tectonics [Fridriksson et al. 2006]. The published CO_2 flux map by Fridriksson et al. [2006] shows a highly localized character of the anomalies, unfortunately, the map does not overlap our study area but we can assume a similar situation. This confirms that geothermal processes are more intense in the areas with the surface manifestation of the alteration, as both are significantly higher compared to the sensors installed in the unaltered areas.

5.3.2 *Sealing Structure*

In the traditional resistivity signature, the low resistivity cap consists of polarizable clay minerals like smectite, corresponding to an anomaly in normalized chargeability. Profiles 1 and 2 have a signal in the normalized chargeability, which is absent in profiles 3 and 4. A distinction can be drawn between a weak (2-3 mS/m) and a strong (8-10 mS/m) signal, similarly as what was found by Troiano et al. [2021]. The weak normalized chargeability (profile 1, 0-180m and profile 2, 0-90m) corresponds to areas with intense surface alteration, as indicated by the shaded regions in Figure 9, which is absent with the strong anomaly (profile 1, 310-355m). Due to the substantial NM difference, we suspect the precipitation of secondary (polarizable) minerals such as iron oxides or sulphides, yielding a stronger signal. These minerals form a shallow sealing structure (Figure 10), restricting the migration of hydrothermal fluids towards the surface and hence prohibiting further alteration. Temperature sensors 7 and 8 do not exhibit elevated temperature, confirming the absence of hydrothermal fluids directly beneath the surface. However, the SP signal shows some erratic anomalies, which can be related to the presence of the (semi-) conductive minerals, fluid flow under the seal, or a combination of the two. The complexity of the SP signal can also be related to 3D effects in the subsurface, where fluid flow patterns are influenced by local geological features and topographic effects (Revil et al. 2023a).

The presence of a sealing structure has major implications on the stability of the field; overpressure can build up under a seal, resulting in hydrothermal explosions [Browne and Lawless 2001]. There is a history of explosive hot-spring activity on the field [Friðleifsson et al. 2003], but it is not well documented. The sealing structure is only identified on profile 1; further mapping and quantification warrant additional field measurements, including higher resolution ERT and IP profiles coupled with permeability measurements [Montanaro et al. 2017].

5.3.3 *Potential and limitations*

The addition of the SP measurements to the ERT allowed us to determine that active hydrothermal processes are present in the shallow part. Profile 1 was measured again two, three, and four months later, Figure 11 shows the resistivity change with the first day. On 26/10/2022, strong variations are present, in the low resistivity areas a significant decrease in resistivity is present, which can be related to an increase in temperature or saturation. The months after that, then intensity of the signal descreased but variations remain present. Time-varying zones are indeed active from a hydrothermal perspective as they are

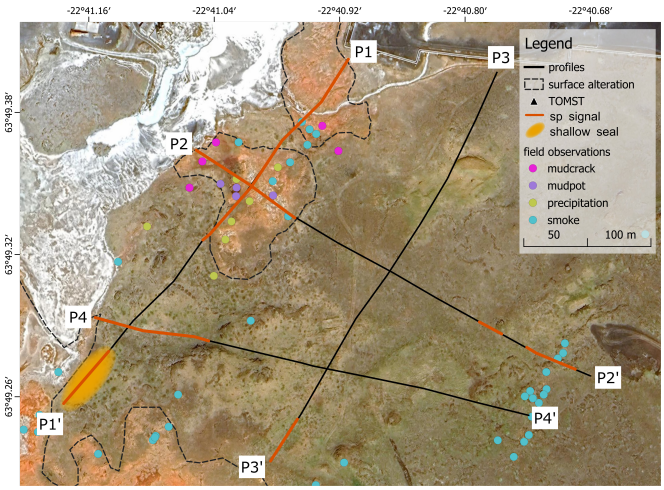

Figure 10: Interpretation of the geophysical signals shown on the profiles. The sp signal represents the circulation of hydrothermal fluids.

zones with higher permeability in which fluids can circulate. Hence, the repeated measurements confirm the interpretation from the static survey. Further investigations of the monitoring signal are out of the scope of this contribution.

The above paragraphs illustrate that by combining ERT, IP, and SP, we are able to identify areas of alteration and hydrothermal activity by using static measurements, and hypothesize the presence of a sealing layer (Figure 10). According to the literature, IP can distinguish between different alteration minerals [e.g. Lévy et al. 2018; Revil et al. 2022]. Textural information can only be quantified through analysis of the frequency-dependence of the polarization response, for instance, through spectral-induced polarization (SIP) measurements. However, if those data were available, it is not an assurance that it could be successfully applied on the field, given the complex nature of volcanic areas [Lévy et al. 2019] and low registered signal-to-noise ratios. A mineralogical analysis is needed to further analyze alteration processes.

The alteration is only identified until 25 to 30 m depth, but this does not exclude that it is not present in deeper parts. Due to the saline nature, the electrolytic conductivity dominates the ERT signal. Indeed Revil et al. [2022] stated that for salinities above 10 S/m the bulk conductivity dominates the surface conductivity, hence chargeability measurements are not reliable, which is coherent with our observations. The salinity at the site is that of seawater, so we can neither confirm nor deny the presence of (alteration) clay below 30 m for this site. This underlines the importance of shallow measurements; in order to retrieve valuable information from the IP signal, an area of freshwater infiltration has to be targeted. Extending the depth of investigation (DOI) would not provide additional information due to the high salinity of the field. Furthermore, the resolution related to a larger DOI might not be sufficient to resolve shallow features such as the seal. Karlsdóttir et al. [2020] reported heterogeneity in the upper layer; our study sheds more light on the type of heterogeneities and closes this knowledge gap. The results from this study are summarized in a conceptual model of the shallow part of the Reykjanes geothermal field (Figure 12) where we show the highly localized nature of geothermal alteration on the field and indicate that shallow and surface observations can potentially be a proxy for deeper processes.

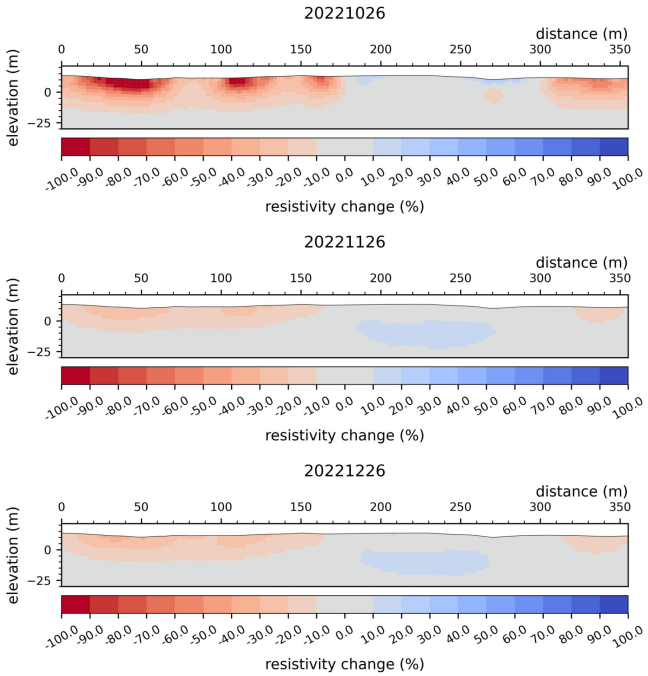

Figure 11: The resistivity change of profile 1 between the measurement shown in Figure 9 and the same profile measured again on 26/10/2022, 26/11/2022 and 26/12/2022. The changes are given in a relative change of resistivity, a positive number reflects an increase and vice versa.

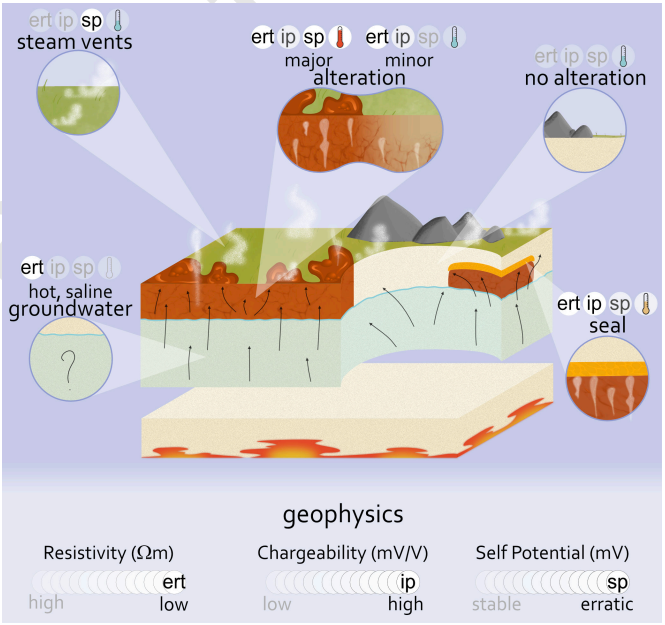

Figure 12: Conceptual model showing the main findings of this research, the different features are indicated alongside the geophysical methods used to identify said features. The brightness of the icons represents the strength of the signal of the parameter. Note that there was no temperature data available in the 'hot saline groundwater' area since the sensors are mounted in the shallow soil. The black arrows represent interpreted fluid flow.

6 Conclusion

In this study, we used geo-electric methods to characterize the shallow electrical signature of the Reykjanes geothermal field and show that study of the near surface can give insight in the state of the geothermal system.

The resistivity structure is that typical of a high temperature geothermal field, and concurs with previous studies where it was found that the capping structure of the geothermal field is highly heterogeneous [Karlsdóttir et al. 2020]. Zones of intense activity are characterized by a low resistivity and a weak, but present signal in the normalized chargeability, due to the presence of alteration clays. The IP data reveals a previously unknown shallow sealing structure, which has the same resistivity signature as the alteration clays of the geothermal cap but a significantly stronger polarization response. This cap prohibits the migration of geothermal fluids towards the surface, resulting in an absence of surface manifestations. Such a seal can be potentially hazardous due to overpressurization, resulting in explosions. The resistivity and chargeability provide information about the geology and maximum progression of geothermal alteration, but on their own carry no information regarding the state of the system. Therefore, we can not conclude whether hydrothermal processes are still ongoing. The addition of the spontaneous potential overcomes this, as it is strongly related to fluid flow mechanisms. Positive SP anomalies are present throughout the area, showing that there is hydrothermal activity in the shallow subsurface but also that it is not limited to the areas with intense alteration. This means that the field is currently still undergoing progressive alteration.

Previous attempts to use resistivity methods to monitor the field were unsuccessful [Darnet et al. 2019] and mainly related to the resolution as they target a large depth (>3km). Our study has a very high resolution at shallow depth, enabling us to capture changes in the system on a short timescale. Given the nature of the site, with the cap of the geothermal system reaching the surface, changes in the shallow cap can be directly related to deeper processes.

At Reykjanes, we show that the combination of ERT, IP, and SP is essential to provide valuable insight into the shallow structures of a geothermal system, which can act as a proxy for deeper processes. Due to the fact that these interpretations can be drawn using limited data, the workflow we present here is widely accessible and easy to implement. Additionally, due to the absence of sampling, the method is completely non-intrusive. We therefore recommend joint application and interpretation of ERT, IP, and SP for complex environments such as volcanoes and geothermal systems.

Author Contributions

LV: survey design, data processing and writing the draft; EV: ERT and SP data processing; WD: IP data processing; AFO: IP data processing and revision of the article; OF: mapping of the site; KJ and BB: coordination and survey design; CC and TH: survey design, revision and project funding. The field campaign was conducted by LV, EV, WD, OF, TH and CC

Acknowledgements

This work is part of the ERupT project, funded by the Flanders Research Foundation (FWO), grant G037222N. We extend our gratitude to the field operator, HS Orka for allowing us to conduct our experiment on their site. We would also like to thank the colleagues at IMO for coordinating the experiment and for their technical assistance on the field. Lastly, we would like to thank Yesim Cubuk Sabuncu, and Hanne de Lathauwer for their assistance during the field campaign.

Data Availability

All new data from the ERupT project have been deposited in the Zenodo repository and are freely accessible at the following link: 10.5281/zenodo.14251329.

Copyright notice

References

Aizawa, K., Y. Ogawa, and T. Ishido (2009). "Groundwater flow and hydrothermal systems within volcanic edifices: Delineation by electric self-potential and magnetotellurics". *Journal of Geophysical Research: Solid Earth* 114(B1). DOI: 10.1029/2008jb005910.

Ardid, A., R. Archer, E. Bertrand, F. Sepulveda, P. Tarits, and D. Dempsey (2021). "Heat Transfer Through the Wairakei-Tauhara Geothermal System Quantified by Multi-Channel Data Modeling". *Geophysical Research Letters* 48(8). DOI: 10.1029/2020gl092056.

Arnason, K., R. Karlsdottir, H. Eysteinsson, Ó. Flóvenz, and S. T. Gudlaugsson (2000). "The resistivity structure of high-temperature geothermal systems in Iceland". In: *Proceedings of the World Geothermal Congress 2000, Kyushu-Tohoku, Japan*, pages 923–928.

Árnason, K. (2015). "The static shift problem in MT soundings". In: *Proceedings world geothermal congress*.

Arnórsson, S. (1995). "Geothermal Systems in Iceland: Structure and Conceptual Models - I. High Temperature Areas". *Geothermics* 24 (5), pages 561–602. DOI: https://doi.org/10.1016/0375-6505(95)00025-9.

Barde-Cabusson, S., A. Finizola, and N. Grobbe (2021). "A practical approach for self-potential data acquisition, processing, and visualization". *Interpretation* 9(1), T123–T143.

Benoit, S., G. Ghysels, K. Gommers, T. Hermans, F. Nguyen, and M. Huysmans (2019). "Characterization of spatially variable riverbed hydraulic conductivity using electrical resistivity tomography and induced polarization". *Hydrogeology Journal* 27 (1), pages 395–407. DOI: 10.1007/s10040-018-1862-7.

Binley, A. and L. Slater (2020). *Resistivity and Induced Polarization - Theory and Applications to the Near-Surface Earth*. cambridge university press. ISBN: 978-1-108-49274-4. DOI: 10.1017/9781108685955.

Björnsson, S., S. Arnórsson, and J. Tómasson (1970). "Exploration of the Reykianes Thermal Brine Area". *Geothermics* 2, pages 1640–1650.

Bretaudeau, F., F. Dubois, S. G. B. Kassa, N. Coppo, P. Wawrzyniak, and M. Darnet (2021). "Time-lapse resistivity imaging: CSEM-data 3-D double-difference inversion and application to the Reykjanes geothermal field". *Geophysical Journal International* 226 (3), pages 1764–1782. DOI: 10.1093/gji/ggab172.

Browne, P. and J. Lawless (2001). "Characteristics of hydrothermal eruptions, with examples from New Zealand and elsewhere". *Earth-Science Reviews* 52(4), pages 299–331. DOI: https://doi.org/10.1016/S0012-8252(00)00030-1.

Caterina, D., J. Beaujean, T. Robert, and F. Nguyen (2013). "A comparison study of different image appraisal tools for electrical resistivity tomography". *Near Surface Geophysics* 11 (6), pages 639–657. DOI: 10.3997/1873-0604.2013022.

Caterina, D., T. Hermans, and F. Nguyen (2014). "Case studies of incorporation of prior information in electrical resistivity tomography: Comparison of different approaches". *Near Surface Geophysics* 12 (4), pages 451–465. DOI: 10.3997/1873-0604.2013070.

Caudron, C., A. Bernard, S. Murphy, S. Inguaggiato, and H. Gunawan (2018a). "Volcano-hydrothermal system and activity of Sirung volcano (Pantar Island, Indonesia)". *Journal of Volcanology and Geothermal Research* 357, pages 186–199. DOI: 10.1016/j.jvolgeores.2018.04.011.

Caudron, C., T. Girona, B. Taisne, Suparjan, H. Gunawan, Kristianto, and Kasbani (2019). "Change in seismic attenuation as a long-term precursor of gas-driven eruptions". *Geology* 47 (7), pages 632–636. DOI: 10.1130/G46107.1.

Caudron, C., B. Taisne, J. Neuberg, A. D. Jolly, B. Christenson, T. Lecocq, Suparjan, D. Syahbana, and G. Suantika (2018b). "Anatomy of phreatic eruptions". *Earth, Planets and Space* 70 (1). DOI: 10.1186/s40623-018-0938-x.

Chaput, M., A. Finizola, A. Peltier, N. Villeneuve, M. Crovisier, and S. Barde-Cabusson (2019). "Where does a volcano break? Using self-potential reiteration to forecast the precise location of major destructive events on active volcanoes: the case study of the Piton de la Fournaise 2007 caldera collapse". *Volcanica*.

Chiodini, G., D. Granieri, R. Avino, S. Caliro, A. Costa, and C. Werner (2005). "Carbon dioxide diffuse degassing and estimation of heat release from volcanic and hydrothermal systems". *Journal of Geophysical Research: Solid Earth* 110(B8). DOI: 10.1029/2004jb003542.

Christenson, B., A. Reyes, R. Young, A. Moebis, S. Sherburn, J. Cole-Baker, and K. Britten (2010). "Cyclic processes and factors leading to phreatic eruption events: Insights from the 25 September 2007 eruption through Ruapehu Crater Lake, New Zealand". *Journal of Volcanology and Geothermal Research* 191(1–2), pages 15–32. DOI: 10.1016/j.jvolgeores.2010.01.008.

Clifton, A. E. and S. A. Kattenhorn (2006). "Structural architecture of a highly oblique divergent plate boundary segment". *Tectonophysics* 419 (1-4), pages 27–40. DOI: 10.1016/j.tecto.2006.03.016.

Cong-Thi, D., L. P. Dieu, D. Caterina, X. De Pauw, H. D. Thi, H. H. Ho, F. Nguyen, and T. Hermans (2024). "Quantifying salinity in heterogeneous coastal aquifers through ERT and IP: Insights from laboratory and field investigations". *Journal of Contaminant Hydrology* 262, page 104322. DOI: https://doi.org/10.1016/j.jconhyd.2024.104322.

Dahlin, T., V. Leroux, and J. Nissen (2002). "Measuring techniques in induced polarisation imaging". *Journal of Applied Geophysics* 50, pages 279–298.

Dahlin, T. and B. Zhou (2004). *A numerical comparison of 2D resistivity imaging with 10 electrode arrays*.

— (2006). "Multiple-gradient array measurements for multichannel 2D resistivity imaging". *Near Surface Geophysics* 4 (2), pages 113–123. DOI: 10.3997/1873-0604.2005037.

Darnet, M., N. Coppo, P. Wawrzyniak, S. Nielsson, G. Fridleifsson, and E. Schill (2019). "Imaging and monitoring the Reykjanes supercritical geothermal reservoir in Iceland with time-lapse CSEM and MT measurements". In: *European Geothermal Congress*. Den Haag, Netherlands.

Deer, W. A. (1978). *Rock-forming minerals*. Volume 3 Sheet Silicates.

Demets, C., R. G. Gordon, D. F. Argus, and S. Stein (1994). "Effect of recent revisions to the geomagnetic reversal time scale on estimates of current plate motions". *Geophysical Research Letters* 21 (20), pages 2191–2194.

Di Maio, R., P. Mauriello, D. Patella, Z. Petrillo, S. Piscitelli, and A. Siniscalchi (1998). "Electric and electromagnetic outline of the Mount Somma-Vesuvius structural setting". *Journal of volcanology and Geothermal Research*.

Dumont, G., T. Pilawski, P. Dzaomuho-Lenieregue, S. Hiligsmann, F. Delvigne, P. Thonart, T. Robert, F. Nguyen, and T. Hermans (2016). "Gravimetric water distribution assessment from geoelectrical methods (ERT and EMI) in municipal solid waste landfill". *Waste Management* 55, pages 129–140. DOI: 10.1016/j.wasman.2016.02.013.

Einarsson, P. (2008). "Plate boundaries, rifts and transforms in Iceland". *Jökull* 58, pages 35–58.

Einarsson, P., V. Eyjólfsson, and Á. R. Hjartardóttir (2023). "Tectonic framework and fault structures in the Fagradalsfjall segment of the Reykjanes Peninsula Oblique Rift, Iceland". *Bulletin of Volcanology* 85 (2). DOI: 10.1007/s00445-022-01624-x.

Evrard, M., G. Dumont, T. Hermans, M. Chouteau, O. Francis, E. Pirard, and F. Nguyen (2018). "Geophysical investigation of the Pb–Zn deposit of Lontzen–Poppelsberg, Belgium". *Minerals* 8 (6). DOI: 10.3390/min8060233.

Eysteinsson, H., K. Árnason, and Ó. G. Flóvenz (1994). "Resistivity methods in geothermal prospecting in Iceland". *Surveys in Geophysics* 15(2), pages 263–275. DOI: 10.1007/BF00689862.

Flores-Orozco, A., J. Gallistl, M. Bücker, and K. H. Williams (2018). "Decay curve analysis for data error quantification in time-domain induced polarization imaging". *Geophysics* 83 (2), E75–E86. DOI: 10.1190/geo2016-0714.1.

Flores-Orozco, A., A. Kemna, and E. Zimmermann (2012). "Data error quantification in spectral induced polarization imaging". *Geophysics* 77 (3). DOI: 10.1190/geo2010-0194.1.

Flóvenz, Ó., G. Hersir, K. Sæmundsson, H. Ármannsson, and Þ. Friðriksson (2012). "7.03 - Geothermal Energy Exploration Techniques". In: *Comprehensive Renewable Energy*. Edited by A. Sayigh. Oxford: Elsevier, pages 51–95. ISBN: 978-0-08-087873-7. DOI: https://doi.org/10.1016/B978-0-08-087872-0.00705-8.

Fowler, A. P., R. A. Zierenberg, P. Schiffman, N. Marks, and G. Ó. Frileifsson (2015). "Evolution of fluid-rock interaction in the Reykjanes geothermal system, Iceland: Evidence from Iceland Deep Drilling Project core RN-17B". *Journal of Volcanology and Geothermal Research* 302, pages 47–63. DOI: 10.1016/j.jvolgeores.2015.06.009.

Friðleifsson, G. Ó., W. A. Elders, R. A. Zierenberg, A. P. Fowler, T. B. Weisenberger, K. G. Mesfin, Ó. Sigurðsson, S. Níelsson, G. Einarsson, F. Óskarsson, E. Á. Guðnason, H. Tulinius, K. Hokstad, G. Benoit, F. Nono, D. Loggia, F. Parat, S. B. Cichy, D. Escobedo, and D. Mainprice (2020). "The Iceland Deep Drilling Project at Reykjanes: Drilling into the root zone of a black smoker analog". *Journal of Volcanology and Geothermal Research* 391, page 106435. DOI: 10.1016/j.jvolgeores.2018.08.013.

Friðleifsson, G. Ó., H. Ármannsson, K. Árnason, I. Þ. Bjarnason, and G. Gíslason (2003). "Iceland Deep Drilling Project (IDDP): Drilling targets for supercritical fluid". In: *Int. Geothermal Conference*.

Fridriksson, T., B. R. Kristjánsson, H. Ármannsson, E. Margrétardóttir, S. Ólafsdóttir, and G. Chiodini (2006). "CO2 emissions and heat flow through soil, fumaroles, and steam heated mud pools at the Reykjanes geothermal area, SW Iceland". *Applied Geochemistry* 21 (9), pages 1551–1569. DOI: 10.1016/j.apgeochem.2006.04.006.

Gasperikova, E., G. Newman, D. Feucht, and K. Arnason (2011). "3D MT characterization of two geothermal fields in Iceland". *GRC Transactions* 35(1-2), pages 1667–1671.

Ghorbani, A., A. Revil, A. Coperey, A. S. Ahmed, S. Roque, M. J. Heap, H. Grandis, and F. Viveiros (2018). "Complex conductivity of volcanic rocks and the geophysical mapping of alteration in volcanoes". *Journal of Volcanology and Geothermal Research* 357, pages 106–127. DOI: 10.1016/j.jvolgeores.2018.04.014.

Grobbe, N. and S. Barde-Cabusson (2019). "Self-Potential Studies in Volcanic Environments: A Cheap and Efficient Method for Multiscale Fluid-Flow Investigations". *International Journal of Geophysics* 2019(1), page 2985824. DOI: https://doi.org/10.1155/2019/2985824.

Gurin, G., K. Titov, Y. Ilyin, and A. Tarasov (2015). "Induced polarization of disseminated electronically conductive minerals: A semi-empirical model". *Geophysical Journal International* 200 (3), pages 1555–1565. DOI: 10.1093/gji/ggu490.

Hermans, T., F. Nguyen, T. Robert, and A. Revil (2014). "Geophysical methods for monitoring temperature changes in shallow low enthalpy geothermal systems". *Energies* 7 (8), pages 5083–5118. DOI: 10.3390/en7085083.

Hermans, T., A. Vandenbohede, L. Lebbe, R. Martin, A. Kemna, J. Beaujean, and F. Nguyen (2012). "Imaging artificial salt water infiltration using electrical resistivity tomography constrained by geostatistical data". *Journal of Hydrology* 438-439, pages 168–180. DOI: 10.1016/j.jhydrol.2012.03.021.

Hermans, T. J. (2014). "Integration of near-surface geophysical, geological and hydrogeological data with multiple-point geostatistics in alluvial aquifers". PhD thesis.

Hersir, G. P., K. Árnason, A. M. Vilhjálmsson, K. Saemundsson, Þ. Ágústsdóttir, and G. Ó. Friðleifsson (2020). "Krýsuvík high temperature geothermal area in SW Iceland: Geological setting and 3D inversion of magnetotelluric (MT) resistivity data". *Journal of Volcanology and Geothermal Research* 391, page 106500. DOI: https://doi.org/10.1016/j.jvolgeores.2018.11.021.

IMO (2024). https://en.vedur.is/ [Accessed: (19/09/2024)].

Kadko, D., K. Gronvold, and D. Butterfield (2007). "Application of radium isotopes to determine crustal residence times of hydrothermal fluids from two sites on the Reykjanes Peninsula, Iceland". *Geochimica et Cosmochimica Acta* 71 (24), pages 6019–6029. DOI: 10.1016/j.gca.2007.09.018.

Karlsdóttir, R., A. M. Vilhjálmsson, and E. Á. Guðnason (2020). "Three dimensional inversion of magnetotelluric (MT) resistivity data from Reykjanes high temperature field in SW Iceland". *Journal of Volcanology and Geothermal Research* 391. DOI: 10.1016/j.jvolgeores.2018.11.019.

Kemna, A. (2000). "Tomographic inversion of complex resisitvity-theory and application." PhD thesis. Bochum, Germany: Ruhr-Universität.

Khodayar, M., S. Björnsson, E. Á. Guðnason, S. Níelsson, G. Axelsson, and C. Hickson (2018). "Tectonic Control of the Reykjanes Geothermal Field in the Oblique Rift of SW Iceland: From Regional to Reservoir Scales". *Open Journal of Geology* 08 (03), pages 333–382. DOI: 10.4236/ojg.2018.83021.

Koestel, J., A. Kemna, M. Javaux, A. Binley, and H. Vereecken (2008). "Quantitative imaging of solute transport in an unsaturated and undisturbed soil monolith with 3-D ERT and TDR". *Water Resources Research* 44 (12). DOI: 10.1029/2007WR006755.

Krmíček, L., V. R. Troll, T. Thordarson, M. Brabec, W. M. Moreland, and A. Maťo (2023). "The 2023 Litli-Hrútur eruption of the Fagradalsfjall Fires, SW-Iceland: Insights from trace element compositions of olivine". *Czech Polar Reports* 13 (2), pages 257–270. DOI: 10.5817/CPR2023-2-20.

Labrecque, D., M. Miletto, W. Daily, A. Ramirez, and E. Owen (1996). "The effects of noise on Occam's inversion of resistivity tomography data". *Geophysics* 61(2), pages 538–548.

LaFemina, P. C., T. H. Dixon, R. Malservisi, T. Árnadóttir, E. Sturkell, F. Sigmundsson, and P. Einarsson (2005). "Geodetic GPS measurements in south Iceland: Strain accumulation and partitioning in a propagating ridge system". *Journal of Geophysical Research: Solid Earth* 110 (11), pages 1–21. DOI: 10.1029/2005JB003675.

Lesmes, D. P. and K. M. Frye (2001). "Influence of pore fluid chemistry on the complex conductivity and induced polarization responses of Berea sandstone". *Journal of Geophysical Research: Solid Earth* 106(B3), pages 4079–4090. DOI: https://doi.org/10.1029/2000JB900392.

Lévy, L., B. Gibert, F. Sigmundsson, D. Deldicque, F. Parat, and G. P. Hersir (2019). "Tracking Magmatic Hydrogen Sulfur Circulations Using Electrical Impedance: Complex Electrical Properties of Core Samples at the Krafla Volcano, Iceland". *Journal of Geophysical Research: Solid Earth* 124 (3), pages 2492–2509. DOI: 10.1029/2018JB016814.

Lévy, L., B. Gibert, F. Sigmundsson, O. G. Flóvenz, G. P. Hersir, P. Briole, and P. A. Pezard (2018). "The role of smectites in the electrical conductivity of active hydrothermal systems: Electrical properties of core samples from Krafla volcano, Iceland". *Geophysical Journal International* 215 (3), pages 1558–1582. DOI: 10.1093/gji/ggy342.

Loke, M., J. Chambers, D. Rucker, O. Kuras, and P. Wilkinson (2013). "Recent developments in the direct-current geoelectrical imaging method". *Journal of Applied Geophysics* 95, pages 135–156. DOI: 10.1016/j.jappgeo.2013.02.017.

Lowrie, W. (2007). *Fundamentals of Geophysics, second edition*.

Magnusdottir, L. and M. T. Jonsson (2020). "Casing-to-casing resistance study performed at Reykjanes geothermal field in Iceland to estimate fracture connectivity". *Geothermics* 88, page 101860. DOI: https://doi.org/10.1016/j.geothermics.2020.101860.

Mansourian, D., A. Vanderhasselt, W. Cornelis, and T. Hermans (2023). "Response to soil compaction of the electrical resistivity tomography, induced polarisation, and electromagnetic induction methods: a case study in Belgium". *Soil Research* 62(1). DOI: https://doi.org/10.1071/SR22260.

Marks, N., P. Schiffman, R. A. Zierenberg, H. Franzson, and G. Ó. Fridleifsson (2010). "Hydrothermal alteration in the Reykjanes geothermal system: Insights from Iceland deep drilling program well RN-17". *Journal of Volcanology and Geothermal Research* 189 (1-2), pages 172–190. DOI: 10.1016/j.jvolgeores.2009.10.018.

Meunier, A. (2005). "Hydrothermal Process — Thermal Metamorphism". In: *Clays*. Berlin, Heidelberg: Springer Berlin Heidelberg, pages 379–415. ISBN: 978-3-540-27141-3. DOI: 10.1007/3-540-27141-4_9.

Minami, T., M. Utsugi, H. Utada, T. Kagiyama, and H. Inoue (2018). "Temporal variation in the resistivity structure of the first Nakadake crater, Aso volcano, Japan, during the magmatic eruptions from November 2014 to May 2015, as inferred by the ACTIVE electromagnetic monitoring system". *Earth, Planets and Space* 70(1), page 138.

Montanaro, C., K. Mayer, R. Isaia, M. Gresse, B. Scheu, T. I. Yilmaz, J. Vandemeulebrouck, T. Ricci, and D. B. Dingwell (2017). "Hydrothermal activity and subsoil complexity: implication for degassing processes at Solfatara crater, Campi Flegrei caldera". *Bulletin of Volcanology* 79(12), page 83.

Montanaro, C., E. Mick, J. Salas-Navarro, C. Caudron, S. J. Cronin, J. M. de Moor, B. Scheu, J. Stix, and K. Strehlow (2022). "Phreatic and Hydrothermal Eruptions: From Overlooked to Looking Over". *Bulletin of Volcanology* 84(6), page 64. DOI: 10.1007/s00445-022-01571-7.

Muñoz, G. (2014). "Exploring for Geothermal Resources with Electromagnetic Methods". *Surveys in Geophysics* 35(1), pages 101–122. DOI: 10.1007/s10712-013-9236-0.

Oldenburg, D. W. and Y. Li (1994). "Subspace linear inverse method". *Inverse Problems* 10 (4), pages 915–935. DOI: 10.1088/0266-5611/10/4/011.

Paepen, M., W. Deleersnyder, S. D. Latte, K. Walraevens, and T. Hermans (2022). "Effect of Groundwater Extraction and Artificial Recharge on the Geophysical Footprints of Fresh Submarine Groundwater Discharge in the Western Belgian Coastal Area". *Water* 14 (7). DOI: 10.3390/w14071040.

Pałgan, D., C. W. Devey, and I. A. Yeo (2017). "Volcanism and hydrothermalism on a hotspot–influenced ridge: Comparing Reykjanes Peninsula and Reykjanes Ridge, Iceland". *Journal of Volcanology and Geothermal Research* 348, pages 62–81. DOI: 10.1016/j.jvolgeores.2017.10.017.

Parasnis, D. S. (1988). "Reciprocity theorems in geoelectric and geoelectromagnetic work". *Geoexploration* 25 (3), pages 177–198. DOI: 10.1016/0016-7142(88)90014-2.

Pelton, W. H., S. H. Wards, P. G. Hallof, W. R. Sills, and P. H. Nelson5 (1978). "Mineral Discrimination and Removal of Inductive Coupling with Multifrequency IP". *Geophysics* 43 (3).

Revil, A. and A. Jardani (2013). *The self-potential method - Theory and Applications in Environmental Geosciences*. Cambridge University Press. ISBN: 978-1-107-01927-0.

Revil, A., A. Finizola, and M. Gresse (2023a). "Self-potential as a tool to assess groundwater flow in hydrothermal systems: A review". *Journal of Volcanology and Geothermal Research* 437. DOI: 10.1016/j.jvolgeores.2023.107788.

Revil, A., A. Finizola, S. Piscitelli, E. Rizzo, T. Ricci, A. Crespy, B. Angeletti, M. Balasco, S. C. Barde, L. Bennati, A. Bolève, S. Byrdina, N. Carzaniga, F. D. Gangi, J. Morin, A. Perrone, M. Rossi, E. Roulleau, and B. Suski (2008). "Inner structure of La Fossa di Vulcano (Vulcano Island, southern Tyrrhenian Sea, Italy) revealed by high-resolution electric resistivity tomography coupled with self-potential, temperature, and CO2 diffuse degassing measurements". *Journal of Geophysical Research: Solid Earth* 113 (7). DOI: 10.1029/2007JB005394.

Revil, A., D. Hermitte, E. Spangenberg, and J. J. Cochemé (2002). "Electrical properties of zeolitized volcaniclastic materials". *Journal of Geophysical Research: Solid Earth* 107 (B8). DOI: 10.1029/2001jb000599.

Revil, A., Y. Qi, N. Panwar, M. Gresse, H. Grandis, R. Sharma, Y. Géraud, N. Chibati, and A. Ghorbani (2022). "Induced polarization images alteration in stratovolcanoes". *Journal of Volcanology and Geothermal Research* 429. DOI: 10.1016/j.jvolgeores.2022.107598.

Revil, A., A. Finizola, T. Johnson, T. Ricci, M. Gresse, E. Delcher, S. Barde-Cabusson, P.-A. Duvillard, and M. Ripepe (2023b). "The thermal plumbing system of Stromboli volcano, Aeolian Islands (Italy) inferred from electrical conductivity and induced polarization tomography". *Journal of Geophysical Research: Solid Earth* 128(6), e2023JB026475.

Robert, T., A. Dassargues, S. Brouyère, O. Kaufmann, V. Hallet, and F. Nguyen (2011). "Assessing the contribution of electrical resistivity tomography (ERT) and self-potential (SP) methods for a water well drilling program in fractured/karstified limestones". *Journal of Applied Geophysics* 75(1), pages 42–53. DOI: https://doi.org/10.1016/j.jappgeo.2011.06.008.

Rosas-Carbajal, M., J.-C. Komorowski, F. Nicollin, and D. Gibert (2016). "Volcano electrical tomography unveils edifice collapse hazard linked to hydrothermal system structure and dynamics". *Scientific Reports* 6(1), page 29899. DOI: 10.1038/srep29899.

Rosenkjaer, G. K., E. Gasperikova, G. A. Newman, K. Arnason, and N. J. Lindsey (2015). "Comparison of 3D MT inversions for geothermal exploration: Case studies for Krafla and Hengill geothermal systems in Iceland". *Geothermics* 57, pages 258–274. DOI: https://doi.org/10.1016/j.geothermics.2015.06.001.

Sæmundsson, K., M. Sigurgeirsson, and G. Ó. Friðleifsson (2020). "Geology and structure of the Reykjanes volcanic system, Iceland". *Journal of Volcanology and Geothermal Research* 391. DOI: 10.1016/j.jvolgeores.2018.11.022.

Sigmundsson, F., P. Einarsson, Á. R. Hjartardóttir, V. Drouin, K. Jónsdóttir, T. Árnadóttir, H. Geirsson, S. Hreinsdóttir, S. Li, and B. G. Ófeigsson (2020). "Geodynamics of Iceland and the signatures of plate spreading". *Journal of Volcanology and Geothermal Research* 391, page 106436. DOI: 10.1016/j.jvolgeores.2018.08.014.

Sigurðsson, F. (1986). "Hydrogeology and groundwater on the Reykjanes Peninsula". *Jökull* 36 (1), pages 11–29. DOI: 10.33799/jokull1986.36.011.

Sigurdsson, Ó. (2010). "The Reykjanes seawater geothermal system–Its exploitation under regulatory constraints". In: *Proceedings WGC*. Bali, Indonesia.

Slater, L., A. Binley, W. Daily, and R. Johnson (2000). "Cross-hole electrical imaging of a controlled saline tracer injection". *Journal of Applied Geophysics* 44, pages 85–102.

Thibaut, R., T. Kremer, A. Royen, B. K. Ngun, F. Nguyen, and T. Hermans (2021). "A new workflow to incorporate prior information in minimum gradient support (MGS) inversion of electrical resistivity and induced polarization data". *Journal of Applied Geophysics* 187. DOI: 10.1016/j.jappgeo.2021.104286.

Thordarson, T. and Á. Höskuldsson (2008). "Postglacial volcanism in Iceland". *Jökull* 58, pages 197–228.

Tikhonov, A. N. and A. Viak (1977). "Solutions of ill-posed problems". *(No Title)*.

Troiano, A., R. Isaia, F. Tramparulo, and M. Di Giuseppe (2021). "The Pisciarelli main fumarole mechanisms reconstructed by electrical resistivity and induced polarization imaging". *Scientific Reports* 11(1), page 18639.

Troiano, A., R. Isaia, M. G. Di Giuseppe, F. D. A. Tramparulo, and S. Vitale (2019). "Deep Electrical Resistivity Tomography for a 3D picture of the most active sector of Campi Flegrei caldera". *Scientific Reports* 9(1), page 15124. DOI: 10.1038/s41598-019-51568-0.

Troll, V. R., F. M. Deegan, T. Thordarson, A. Tryggvason, L. Krmíček, W. M. Moreland, B. Lund, I. N. Bindeman, Á. Höskuldsson, and J. M. Day (2024). "The Fagradalsfjall and Sundhnúkur Fires of 2021–2024: A single magma reservoir under the Reykjanes Peninsula, Iceland?" *Terra Nova*. DOI: 10.1111/ter.12733.

Tsourlos, P. I., J. E. Szymanski, and G. N. Tsokas (1999). "The effect of terrain topography on commonly used resistivity arrays". *Geophysics* 64(5), pages 1357–1363.

Van Riet, B., S. Six, K. Walraevens, A. Vandenbohede, and T. Hermans (2022). "Assessing the Impact of Fractured Zones Imaged by ERT on Groundwater Model Prediction: A Case Study in a Chalk Aquifer in Voort (Belgium)". *Frontiers in Water* 3. DOI: 10.3389/frwa.2021.783983.

Volpi, G., A. Manzella, and A. Fiordelisi (2003). "Investigation of geothermal structures by magnetotellurics (MT): an example from the Mt. Amiata area, Italy". *Geothermics* 32(2), pages 131–145. DOI: https://doi.org/10.1016/S0375-6505(03)00016-6.

Weller, A., L. Slater, and S. Nordsiek (2013). "On the relationship between induced polarization and surface conductivity: Implications for petrophysical interpretation of electrical measurements". *Geophysics* 78 (5). DOI: 10.1190/GEO2013-0076.1.

Wild, J., M. Kopecký, M. Macek, M. Šanda, J. Jankovec, and T. Haase (2019). "Climate at ecologically relevant scales: A new temperature and soil moisture logger for long-term microclimate measurement". *Agricultural and Forest Meteorology* 268, pages 40–47. DOI: 10.1016/j.agrformet.2018.12.018.